Validation of Ultrasonic Image Boundary Recognition in Abdominal Aortic Aneurysm

R. Ravhon, D. Adam*, *Senior Member*, and L. Zelmanovitch

***Abstract*—An aneurysm of the abdominal aorta (AAA) is characterized by modified wall properties, and a balloon-like area usually filled by a thrombus. A rupture of an aortic aneurysm can be fatal, yet there is no way to accurately predict such an occurrence. The study of the wall and thrombus cross-sectional distension, due to a pressure wave, is important as a way of assessing the degradation of the mechanical properties of the vessel wall and the risk of a rupture. Echo ultrasound transverse cross-sectional imaging is used here to study the thrombus and the aortic wall distension, requiring their segmentation within the image. Polar coordinates are defined, and a search is performed for minimizing a cost function, which includes a description of the boundary (based on a limited series of sine and cosine functions) and information from the image intensity gradients along the radii. The method is based on filtering by a modified Canny–Deriche edge detector and then on minimization of an energy function based on five parts. Since echoes from blood in the lumen and the thrombus produce similar patterns and speckle noise, a modified version for identifying the lumen-thrombus border was developed. The method has been validated by various ways, including parameter sensitivity testing and comparison to the performance of an expert. It is robust enough to track the lumen and total arterial cross-sectional area changes during the cardiac cycle. In 34 patients where sequences of images were acquired, the border between the thrombus and the arterial wall was detected with errors less than 2%, while the lumen-thrombus border was detected with a mean error of 4%. Thus, a noninvasive measurement of the AAA cross-sectional area is presented, which has been validated and found to be accurate.**

***Index Terms*—Aortic aneurysm, echo ultrasound, edge detection, image processing.**

I. Introduction

AN abdominal aortic aneurysm (AAA) is the 13th major cause of death in the United States [6], [39] but it has never attracted as much research as other widespread diseases. An AAA is diagnosed when an increase of more than 50% of the aortic diameter is detected relative to a normal healthy diameter. There is a high probability of a rupture with AAA, with an extremely high degree of mortality. The risk of fatality in surgery to repair an aneurysm is also very high [6], [39]. Thus, the decision whether to operate, with the risks involved, or delaying the intervention with the danger of a sudden rupture, is crucial. Unfortunately, in most cases today the decision is based on a single criterion—the aortic diameter.

Several investigators have reported on their efforts to better assess the risk of rupture by attempting to measure the aortic compliance [17], [18], [22], [23], [25], [30], [32], [34], [37], [38], [40], [41]. The estimation of the aortic compliance enables assessment of the mechanical properties of the arterial wall and the stress in the aortic wall. Since in most cases thrombus fills up the aortic cavity, except for a lumen of a normal size in which the blood flows, the effects of the thrombus on wall compliance should also be studied. There are numerous studies that report on changes of the mechanical properties of the arterial wall in AAA [6], [30], [34], [39]–[41].

Ultrasound (US) imaging is a common, relatively inexpensive modality [5]. It can provide high-quality images when used invasively (termed intravascular ultrasound (IVUS) [7], [43]), but the risks involved significantly limit its usage, specifically in AAA patients where rupture can abruptly occur [3]. This imaging modality, when used noninvasively, allows high acquisition rates and provides images in real-time, but the images are corrupted by a high level of noise. This noise makes it difficult to accurately identify edges, since in some regions the noise produces artificial edges, while in other regions there are no echoes present and the edges seem ambiguous. In such low-quality images (which are very common in US imaging), generic algorithms do not identify the border accurately.

Several algorithms have been reported, which could help identify edges in US images [2], [4], [10], [13], [15], [23], [32], [38]. Studies that are focused on the processing of cardiac US images [1], [12], [19] are also of value, since many of the methods are similar. Some of these studies are based on "temporal active contours" [24] or "deformable contour" [27], some on the "snakes" algorithm [26], [42] that defines an object function, also called "energy" function, which is minimized to obtain the estimated border. This "energy" function is divided into two distinct parts, internal and external energies: the internal energy is contour dependent, and it is used to penalize a contour that is not smooth, or one that deviates from *a priori* information [10], [29], [35]. The external energy is a function of the image, and many such examples have been reported [21], [26]. The external energy can also integrate directional information into the edge detection process [9]. The global minimum of this energy function is supposed to be the desired border, but there is no guarantee that this is the correct border. By minimizing this energy function, the authors of many of the

Manuscript received December 7, 1999; revised May 5, 2001. This work was supported by the fund for the promotion of research at the Technion—Israel Institute of Technology, Haifa Israel. The Associate Editor responsible for coordinating the review of this paper and recommending its publication was A. Amini. *Asterisk indicates corresponding author.*

R. Ravhon is with the Department of Biomedical Engineering, Technion—Israel Institute of Technology, Haifa 32000, Israel.

*D. Adam is with the Department of Biomedical Engineering, Technion—Israel Institute of Technology, Haifa 32000, Israel (e-mail: dan@biomed.technion.ac.il).

L. Zelmanovitch is with the Vascular Surgery Department, Sourasky Medical Center, Tel-Aviv 64239, Israel.

Publisher Item Identifier S 0278-0062(01)06584-3.

above reports tried to reach the global minimum: some used finite elements with finite difference calculations [14], while others used dynamic programming [2]. Some reports claim that their methods found the global minimum [20].

The golden standard algorithm for detection of edges in images was reported several years ago by Canny [9]. In that case, the edge is defined as a step function embedded in white noise. But in US images, the data used here, the noise is speckle noise, which has a high degree of correlation. The edge cannot be described by a step function, and the difference in the average gray levels of the various regions is high. Canny suggested using an edge detector, a filter with an impulse response of the first derivative of a Gaussian function, with a given standard deviation (SD). The filter design allows a tradeoff between the signal-to-noise ratio (SNR) and the ability to locate accurately the edge (i.e., resolution), leading to the use of a filter bank, each filter in a different resolution, with the final edge located by some integration of the outputs of these filters (multiresolution) [8]. The algorithm reported here implements these ideas. Another important suggestion was made by Canny [9], i.e., to include information on the edge orientation, which can be accomplished by an edge detector, sensitive to the direction of the edge. Mallat [33] suggested a way to combine multiresolution approach with the edge direction information, and has also shown the use of wavelets for the creation of multiresolution images. These suggestions may well serve as an excellent first stage in the development of robust detector of the borders of organs or geometrical shapes in ultrasound images and, thus, they are implemented here as described below.

The purpose of this study is, therefore, twofold: First, design a robust method for detection of the border between the thrombus and the arterial wall, and for the detection of the border between the thrombus and the arterial lumen. Second, study the changes in arterial lumen area and total arterial cross-sectional area during the cardiac cycle. The scale of these area changes may help understand the alteration of the mechanical properties that the arterial wall undergoes due to AAA, and provide the basis for the hypothesis that very small area changes during the cardiac cycle may indicate fibrotic wall and higher probability of aortic rupture.

II. Methods

The different steps of the algorithm presented here are depicted in Fig. 1. The video image data is given in Cartesian coordinates. The first step is the transformation of this coordinate system to a polar coordinate system, which was found to be simpler [36] for the procedures performed below. The transformation can be expressed by

$$\begin{aligned} x^c(\varphi) &= x_c + r(\varphi)\cdot\cos(\varphi) \\ y^c(\varphi) &= y_c + r(\varphi)\cdot\sin(\varphi) \end{aligned} \tag{1}$$

where

x_c and y_c coordinates of the origin of the polar coordinate system;

$\varphi \in [0, 2\cdot\pi]$ angle with respect to the positive x-axis;

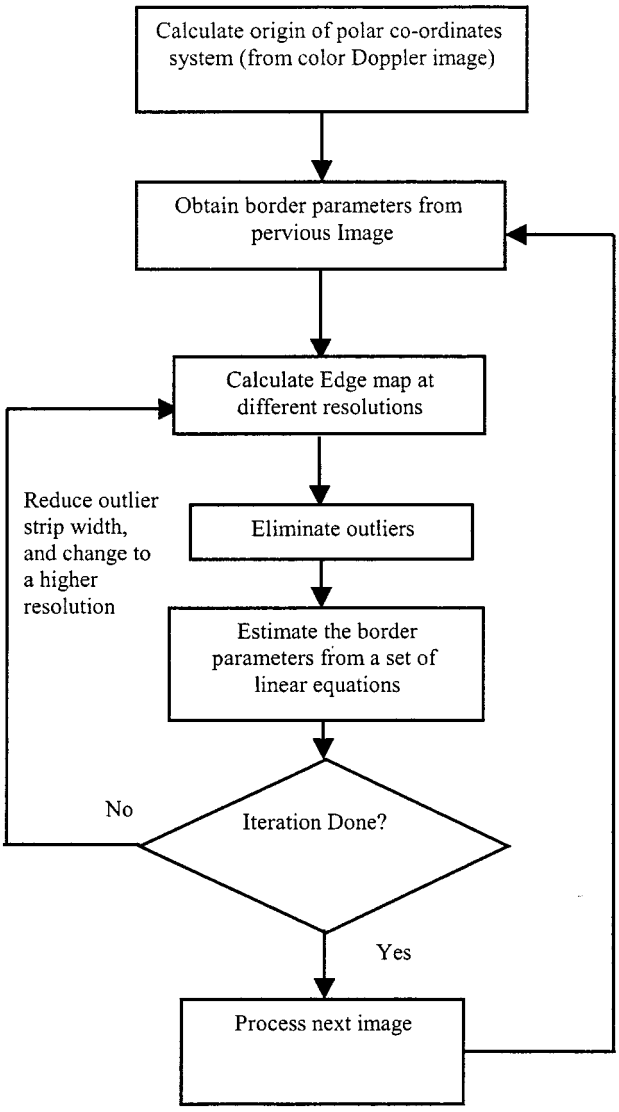

Fig. 1. Flow chart of the main steps of the algorithm. The initial values of all the parameters are given in Tables I and II. All other parameters are set to zero.

$r(\varphi)$ radial distance between the origin and any given point.

This distance is nonnegative. x^c and y^c are the points in which the border is defined. Since the border is a one-dimensional entity, it can be represented by a single function $r(.)$, For the case presented here, an assumption is made: the border must be star shaped. The function $r(.)$ is represented by a Fourier series, as described in (2), where the angle φ is the independent variable

$$\begin{aligned} r(\varphi) = r_0 &+ \sum_n A_n\cdot\cos(n\cdot\varphi) \\ &+ B_n\cdot\sin(n\cdot\varphi), \quad n = 1\cdots M \end{aligned} \tag{2}$$

where M is the maximal number of harmonics selected, r_0, $A_n, B_n;\ n = 1\cdots M$ are the parameters that represent the border. This representation was chosen for the following reasons.

- The function is continuous between the angles 0 and 2π (where the border begins and ends), and also smooth in all its derivatives, at each point.

- The series can be expanded by any number of elements, with a high number for better accuracy, and a small number (harmonics) for better robustness.
- There is no need to predetermine a limitation on the smoothness and continuity, as required when a polynomial representation of the border is used. Also, the condition number of the sensitivity matrix is very low, while it is high in the polynomial representation.

A. MultiResolution Approach

A multiresolution approach [6], [31] greatly enhances the capabilities of the algorithm since initially the border is coarsely approximated, making the algorithm more robust. Near the desired border the smoothing could be relaxed for a more accurate assessment of the border.

The search for an edge should be in the normal direction of the perimeter of the estimated organ border. This can be done by utilizing the information of the edge orientation as part of the external energy [9], [21], [26]

$$E_{\text{line}} = \int (\nabla I_1 \cdot n_\perp) \cdot ds \tag{3}$$

with the integration performed along a closed line in the image, a line that is considered to be the edge. I_1 are the image gray level values, and $n_\perp$ is a unit-vector in the direction perpendicular to the border (and line of integration). The integrand here is simply a directional derivative.

B. Radial Derivative in Polar Coordinates

Two basic assumptions were used here, 1) the border is roughly circular in shape and 2) the origin is approximately in the center. Therefore, the unit-vectors perpendicular to the border orientation are assumed to be radially oriented and the integrand is the radial derivative of the image intensity in the polar coordinate system [19], [36].

As a first step (see flow chart depicted in Fig. 1), the intensities of the US image are normalized to the range between the values zero to one. A discrete grid is defined by the polar coordinate system of (4)

$$\begin{aligned} \rho &= R_{\min} \cdots R_{\max} \\ \phi_n &= \frac{2\pi n}{N}, \quad n = 1 \cdots N \end{aligned} \tag{4}$$

where ρ is the radial distance from the origin, and $R_{\min}$ and $R_{\max}$ are the minimal and maximal expected distances from the origin. Usually, $R_{\min}$ is set to be zero and $R_{\max}$ is the maximal possible distance within the analyzed image. ϕ_n is the angle measured counterclockwise from the X axis, and N is the number of the radial lines; in this case, 128.

Two matrices are used to calculate the Cartesian position of each point on the grid as defined by (5)

$$\begin{aligned} x^p_{i,j} &= x_c + \rho_j \cdot \cos(\phi_i) \\ y^p_{i,j} &= y_c + \rho_j \cdot \sin(\phi_i). \end{aligned} \tag{5}$$

After bilinear interpolation of the gray levels within the image, the results are given in matrix $\text{gr}(m,n)$, which describes the image in the polar coordinate system.

The image in polar coordinates is derived by convolution with the first derivative of a Gaussian. Since the image in the polar representation is not isotropic, the Gaussian SD is different in the radial and the tangential directions.

The implementation is done by a modified Canny–Deriche edge detector[16], with the derivative applied in the radial direction and the smoothing operation applied in the tangential direction. The smoothing operation is applied since the distance of the border from the origin is known to change gradually, enhancing the robustness of the algorithm.

In order to produce a continuous multiresolution scheme, the kernel must be modified at each iteration (Fig. 1), with a ratio between the radial smoothing α_{rad} and the tangential smoothing α_{ang} chosen as

$$\alpha_{\text{ang}} = \alpha_{\text{ratio}} \cdot \alpha_{\text{rad}} \tag{6}$$

and the smoothing level changed according to the progress of the iteration

$$\alpha_{\text{rad}} = \frac{\alpha_A}{\alpha_A \cdot \alpha_B + sd_{\text{brd}}} \tag{7}$$

where α_A and α_B are parameters. sd_{brd} is the degree of fit of the points (used in the above calculations for describing the edge) to the imaged border, as described by (8)

$$sd_{\text{brd}} = \frac{\sqrt{\sum_{i=1}^{D} w_i^{(1)} \left(r_i - \hat{r}(\theta_i)\right)^2}}{D - 2 \cdot M - 1} \tag{8}$$

where r_i is the radial distance of point i from the origin, and $\hat{r}(\cdot)$ is the distance from the origin of the estimated border at this angle (θ_i). θ_i is the angle between the vector to this point (measured counterclockwise) and the X axis, where $i = 1 \cdots D$, and $w_i^{(1)}$ is the radial derivative of the image values (i.e., its gray levels), corresponding to this point. D is the number of points being processed.

C. The Estimation of the Border

In order to save computation time, only the upper 20% of the gradient values are being processed, with these limits being recalculated at each iteration, i.e., the points processed (at each iteration) are at a distance less than SD pixels from the estimated border. SD is defined by (8). These limits are imposed on the first iteration, assuming the SD to be 30 pixels in size, with the border taken as the one estimated at the previous image in that sequence. At the first iteration of the first image, SD is infinite. At each iteration, sd_{brd} decreases. When the calculated decrease is less than a pixel in size, the sd_{brd} used is one less than the previous one.

The border could also be defined in a matrix form

$$r(\varphi) = x(\varphi) \cdot \beta \tag{9}$$

where

$$\begin{aligned} \beta &= [r_0, A_1, \ldots, A_M, B_1, \ldots, B_M]^{\text{T}} \\ x(\varphi) &= \Big[1, \cos(1 \cdot \varphi), \cos(2 \cdot \varphi), \ldots, \\ &\qquad \ldots \cos(M \cdot \varphi), \sin(1 \cdot \varphi), \ldots, \sin(M \cdot \varphi)\Big] \end{aligned}$$

where M is the number of the Fourier harmonics used, and the vector components A_M and B_M are the parameters to be estimated. Finally, an energy function (i.e., an object or an error function) is defined, which should be minimized with respect to β. This energy function is composed of five components, as shown in (10)

$$E = E_1 + E_2 + E_3 + E_4 + E_5. \tag{10}$$

1) The first energy component [defined by (11)], describes the match of the border in the image to the points selected, with the significance (weight) of each point according to the radial derivative

$$E_1 = \sum_{i=1}^{D} w_i^{(1)} \cdot (r_i - r(\theta_i))^2 \tag{11}$$

where D is the number of points processed. This energy component is actually a weighted least square (WLS) formulation, calculated for the image points, which are used as data points, while the border is formulated by (9), with the radial derivative serving as the weight.

2) The second energy function component is given by

$$E_2 = \sum_{i=1}^{N} w^{(2)} \cdot (0 - \dot{r}(\phi_i))^2 \tag{12}$$

which is an approximation of $\int_0^{2\cdot\pi} [\dot{r}(\phi)]^2 d\phi$.

This energy component is similar to the function termed "Snakes" or "active contours" [19], [24], [26], which penalizes an irregular boundary, and is commonly used to reduce the attraction of the dynamic curve to noisy areas that contain high-intensity derivatives. Here the smoothness of the boundary is intrinsic, and this component is used to prevent the boundary from being attracted to areas within the image with high intensities, but far away from the real border.

The angle ϕ_i is evenly distributed

$$\phi_i = \frac{2\pi i}{N}, \quad i = 1 \cdots N. \tag{13}$$

3) The third energy component is defined in a format similar to (12), and is also a standard energy component in the "Snakes" formulation. It provides a smoother border [19], [26]

$$E_3 = \sum_{i=1}^{N} w^{(3)} \cdot (0 - \ddot{r}(\phi_i))^2 \tag{14}$$

which is an approximation of

$$\int_0^{2\cdot\pi} [\ddot{r}(\phi)]^2 d\phi.$$

4) Because of the high acquisition frame rate of the US imaging system, it can be assumed that only small changes occur in between any two consecutive images within a temporal sequence. This assumption was found to hold even for mid-range imaging systems with a relatively slow frame rate. The information that the borders in consecutive images should be similar can be integrated into this energy function as

$$E_4 = \sum_{i=1}^{2\cdot M+1} w^{(4)} \cdot (\beta_i - \beta_i^p)^2 \tag{15}$$

where β^p is the vector of parameters of the border in the previously evaluated image within the sequence and M is the number of the Fourier harmonics used.

5) A bias toward inflation of the border is described similar to the formulation given in [13]

$$E_5 = w^{(5)} \cdot (\beta_1 - 0)^2. \tag{16}$$

All of the energy components described above, may be rewritten as

$$\begin{aligned} E =& E_1 + E_2 + E_3 + E_4 + E_5 \\ =& \sum_{i=1}^{D} w_i^{(1)} \cdot \left(r_i^{(1)} - x_i^{(1)} \cdot \beta\right)^2 \\ &+ \sum_{i=1}^{N} w^{(2)} \cdot \left(r_i^{(2)} - x_i^{(2)} \cdot \beta\right)^2 \\ &+ \sum_{i=1}^{N} w^{(3)} \cdot \left(r_i^{(3)} - x_i^{(3)} \cdot \beta\right)^2 \\ &+ \sum_{i=1}^{2\cdot M+1} w^{(4)} \cdot \left(x_i^{(4)} \cdot \hat{\beta} - r_i^{(4)}\right)^2 \\ &+ w^{(5)} \cdot \left(x_i^{(5)} \cdot \beta - r_i^{(5)}\right)^2. \end{aligned} \tag{17}$$

A different, compact formulation of (17) is given by

$$E = (\bar{r} - X \cdot \beta)^{\mathrm{T}} \cdot W \cdot (\bar{r} - X \cdot \beta) \tag{18}$$

and the following description [see (19)–(24)] details the different components of this compact formulation.

1) The terms in X [in (18)] that relate to the first energy component are

$$\begin{aligned} x_i^{(1)} = [&1, \cos(1 \cdot \theta_i), \cos(2 \cdot \theta_i), \ldots, \cos(M \cdot \theta_i), \\ &\sin(1 \cdot \theta_i), \ldots, \sin(M \cdot \theta_i)] \end{aligned} \tag{19}$$

where θ_i is the angle of a radial ray with regard to the positive direction of the X axis, corresponding to the point of index i. The values of the radial derivatives are given by: $w_i^{(1)}, i = 1, \ldots, D$, with $r_i^{(1)} = r_i$ being the radial distance of point i from the origin.

The weights are corrected by the weights of the first energy term

$$W_{\mathbf{all}} = \sum_{i=1}^{D} \left(W_i^{(1)}\right)^2. \tag{20}$$

The high degree of robustness of the algorithm is achieved by initially introducing a high degree of regularization, and later gradually relaxing the regularization. This is done by multiplying all energy components by sd_{brd}^3.

2) The terms in X [in (18)] that relate to the second energy component are

$$x_i^{(2)} = [1, -1 \cdot \sin(1 \cdot \phi_i), -2 \cdot \sin(2 \cdot \phi_i), \ldots, - M \cdot \sin(M \cdot \phi_i), 1 \cdot \cos(1 \cdot \phi_i), \ldots, M \cdot \cos(M \cdot \phi_i)] \quad (21)$$

with the coefficient: $w^{(2)} = sd_{\text{brd}}^3 \cdot \alpha_{\text{fd}}/N \cdot W_{\text{all}}$; and also: $r_i^{(2)} = 0, i = 1, \ldots, N$.

3) Similarly, the terms in X [in (18)] that relate to the third energy component are

$$x_i^{(3)} = \Big[1, -1^2 \cdot \sin(1 \cdot \phi_i), -2^2 \cdot \sin(2 \cdot \phi_i), \ldots, - M^2 \cdot \sin(M \cdot \phi_i), 1^2 \cdot \cos(1 \cdot \phi_i), \ldots, M^2 \cdot \cos(M \cdot \phi_i)\Big] \quad (22)$$

with the coefficient: $w^{(3)} = sd_{\text{brd}}^3 \cdot \alpha_{\text{sd}}/N \cdot W_{\text{all}}$; and also: $r_i^{(3)} = 0, i = 1, \ldots, N$.

4) The terms in X [in (18)] that relate to the fourth energy component are

$$x_i^{(4)} = [0, \ldots, i, \ldots, 2 \cdot M + 1] \quad (23)$$

with the coefficient: $w^{(4)} = sd_{\text{brd}}^3 \cdot \alpha_{\text{rep}}/(2 \cdot M + 1) \cdot W_{\text{all}}$; and also: $r_i^{(4)} = \beta_i^p, i = 1, \ldots, 2 \cdot M + 1$

5) The terms in X [in (18)] that relate to the fifth energy component are

$$x_i^{(5)} = [1, 0, \ldots, 0] \quad (24)$$

with the coefficient: $w^{(5)} = -\alpha_{\text{inf}} \cdot W_{\text{all}} \cdot sd_{\text{brd}}^3$; and also: $r_i^{(5)} = 0$, with alpha as a parameter.

The sum of all the energy components (see (17)), can then be rewritten in a standard WLS formulation as given in (18) where the equation shown at the bottom of the page holds.

Minimization of the total error function E with respect to β, produces the global minimum $\hat{\beta}$

$$\hat{\beta} = \left\{X^{\text{T}} \cdot W \cdot X\right\}^{-1} \cdot X^{\text{T}} \cdot W \cdot \bar{r} \quad (25)$$

where $\hat{\beta}$ represents the estimated border.

After the border between the arterial wall and the thrombus are determined in a certain image, the origin of the polar coordinate system is recalculated, with the integration path in (26) performed along the whole border

$$x_c^{\text{new}} = \frac{\int_L x^c ds}{\int_L ds}; \quad y_c^{\text{new}} = \frac{\int_L y^c ds}{\int_L ds}. \quad (26)$$

The process of estimating the thrombus-blood border requires some modification of the equations above. This is because both the thrombus region and the blood region are characterized by low gray-level values. Therefore, a Gamma correction was found to be appropriate, which is implemented in the following manner, as described in (27)–(29):

$$Z = \mu_{\text{im}} + \sigma_{\text{im}} \quad (27)$$

$$\text{pic1} = \begin{cases} \text{pic} - Z & \text{pic} \geq Z \\ 0 & \text{pic} < Z \end{cases} \quad (28)$$

$$\text{out}(\text{pic1}) = \frac{1 - e^{-\alpha_{\text{inner}} \cdot (\text{pic1})}}{1 - e^{-\alpha_{\text{inner}}}} \quad (29)$$

where "pic" denotes the original image and "out" denotes the image after transformation. μ_{im} is the estimated average of pixel intensities, calculated over a region of interest (ROI) of 11×11 pixels around the origin, and σ_{im} is the SD estimation of the pixel intensities at the same ROI. Z serves as the lower (intensity) threshold, and "pic1" is the image after the subtraction of this threshold level (for positive values). "out(pic1)" of (29) stretches the linear range of the image intensities. This nonlinear input–output relationship increases significantly the low gray-level values, and only a bit the high gray-level values.

TABLE I
THE PARAMETERS COMMON TO BOTH BORDERS

Parameter	Value
M	6
α_{ratio}	4
α_{A}	6
α_{B}	0.6
ε	3

D. Convergence of the Algorithm

Total error calculations are performed until the SD is found to be low enough: $sd_{\text{brd}} < \varepsilon$. The following error criterion is defined, ϵ_{rad}, the error measured between two contours—the one calculated by the algorithm and the one drawn by the expert. It is stated in the polar coordinate system, describing the mean square error, as shown in (30):

$$\varepsilon_{\text{rad}} = 100 \cdot \frac{\sqrt{\frac{1}{2 \cdot \pi} \cdot \int_0^{2 \cdot \pi} \left(r_{\text{cmp}}(\varphi) - r_{\text{alg}}(\varphi)\right)^2 d\varphi}}{\int_0^{2 \cdot \pi} r_{\text{cmp}}(\varphi)\, d\varphi} \quad (30)$$

where $r_{\text{cmp}}(\cdot)$ is the radial distance of the border from the origin, depending on the polar angle as calculated from the x-axis, and $r_{\text{alg}}(\cdot)$ is that distance, calculated by the algorithm.

$$X = \left[x_1^{(1)} \quad \cdots \quad x_D^{(1)} \quad x_1^{(2)} \quad \cdots \quad x_N^{(2)} \quad x_1^{(3)} \quad \cdots \quad x_N^{(3)} \quad x_1^{(4)} \quad \cdots \quad x_{2 \cdot M+1}^{(4)} \quad x_1^{(5)}\right]^{\text{T}}$$

$$W = \text{diag}\left(\left[w_1^{(1)}, \ldots, w_D^{(1)}, w_1^{(2)}, \ldots, w_N^{(2)}, w_1^{(3)}, \ldots, w_N^{(3)}, w_1^{(4)}, \ldots, w_{2 \cdot M+1}^{(4)}, w_1^{(5)}\right]\right)$$

$$\bar{r} = \left(r_1^{(1)}, \ldots, r_D^{(1)}, r_1^{(2)}, \ldots, r_N^{(2)}, r_1^{(3)}, \ldots, r_N^{(3)}, r_1^{(4)}, \ldots, r_{2 \cdot M+1}^{(4)}, r_1^{(5)}\right)$$

TABLE II
THE PARAMETERS USED FOR EACH OF THE BORDERS

The Parameter	The blood-thrombus border	The border between thrombus and the arterial wall
α_{fd}	10^{-6}	10^{-5}
α_{sd}	10^{-6}	0
α_{rep}	10^{-9}	10^{-7}
α_{inf}	10^{-8}	$2{\cdot}10^{-6}$
α_{inner}	20	20

The sensitivities of the parameters are estimated, as detailed in Section III. The processing described above is done off-line. The algorithm was written in a Matlab environment (Matlab V. 5.2, Mathworks, Inc.). The first image in a sequence requires about six iterations for the algorithm to converge: for the other images in the sequence, it takes only 3–4 iterations to converge. A sequence of 31 images usually requires about 15 min to run on a Pentium processor (200-MHz).

III. RESULTS

The algorithm requires a set of parameters, which are used as coefficients in the different equations. Some of these parameters were selected by trial and error, some by *a priori* information. The parameters used in the equations, as detailed in the Methods Section, are listed in Tables I and II. These sets of parameters were used for generating all the borders in all the image sequences available in this study, and can be used in any other similar image sequences. The algorithm was applied to 34 sequences of ultrasound images, recorded from 34 patients. For each of these sequences, an expert traced the last frame. The results of applying the processing procedure, i.e., the borders detected by the automatic procedure, were compared with tracings made by the expert. A typical image, with the two borders marked by dots, is depicted in Fig. 2(a). The other plots in this figure describe the time sequence changes (during the cardiac cycle) of the cross-sectional areas of the lumen [Fig. 2(b)], the aorta [Fig. 2(c)], and the thrombus area [Fig. 2(d)].The tracings of the borders, made by an expert (a vascular surgeon) on the last frame of each sequence, are considered as the "gold standard" in this study. The discrepancies between these manual tracings and those produced by the algorithm are defined as the error, described in (30). The errors for each image in the whole set of 34 sequences are displayed as histograms in Fig. 3.

The sensitivities of the parameters of the algorithm were tested in several ways: First, the algorithm was tested for its sensitivity to displacement of the origin of the polar coordinate system. The error between the borders detected by the algorithm when the origin is misplaced, and the borders detected when the origin is at the center (which serves as reference), are calculated by (30). The displacement of the origin is given in pixels, where 27 pixels $=$ 1 cm in the tested image sequences. The results are compared with the tracings made by an expert. The results of this sensitivity study are depicted in Fig. 4, for the border between the lumen and the thrombus. In Fig. 4(a), an asterisk marks the location of the origin used by the algorithm, while a gray rectangle marks the region through which the origin was displaced. The plot in Fig. 4 depicts the error [in millimeters] of estimating the location of the lumen-thrombus border, as the function of the horizontal and vertical shifts of the origin [in pixels], in relation to the location of the border when the origin is at the center of the lumen. The sensitivity of detection of the border between the thrombus and the arterial wall to displacement of the origin, is depicted in Fig. 5. In Fig. 5(a), an asterisk marks the location of the origin used by the algorithm, while a gray rectangle marks the region through which the origin was displaced. In Fig. 5(b), the plot is of the error [in millimeters] of estimating the location of the thrombus-arterial wall border, as the function of the horizontal and vertical shifts of the origin [in pixels], in relation to the location of the border, calculated when the origin is at the center of the lumen.

The sensitivity of the algorithm to its parameters was measured by calculating the error between the border found when the optimal parameters are used [with results as seen in Fig. 2(a)] and the border found when modified parameters are used. This measurement was performed for the last frame in each sequence. All tested parameters were changed (one at a time) by up to $\pm$50%. The errors in estimating the border, when the different parameters are changed by $\pm$50%, are calculated separately for the border between the lumen and the thrombus, and for the border between the thrombus and the arterial wall, as tabulated in Table III.

In Fig. 6, the SD of the length is depicted, of the border along the aortic cross section circumference, versus the diameter of the aorta. It is calculated over the sequence of the image frames, i.e., during the cardiac cycle, and normalized by the mean circumference. The maximal pulsatility movement is depicted in Fig. 8(a), together with the minimal pulsatility movement [Fig. 8(b)]. These values are calculated by selecting the maximal (and minimal) ratios over the sequence of the images along the cardiac cycle. The maximal and minimal values are selected from the SD of the length of the border along the sector circumference and the mean length.

A. The Pulsatility Movement Measure

The most common clinical measure of AAA severity, which plays a major role in making the decision on surgical intervention, is the diameter of the aneurysm. Therefore, the results of

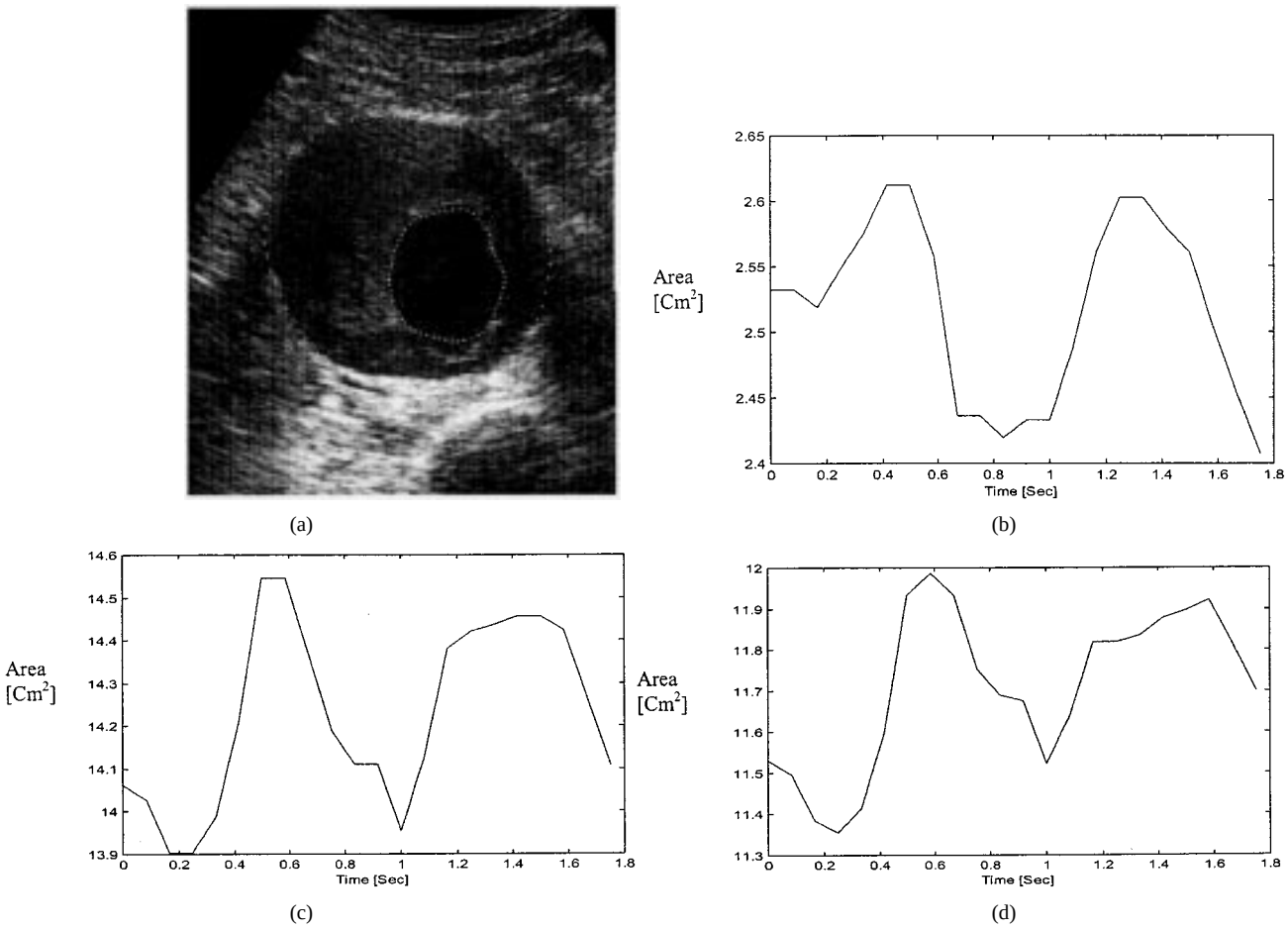

Fig. 2. (a) A typical ultrasound image of cross section of the abdominal aorta, with the borders identified by the algorithm marked by dots. (b) A plot describing the time sequence changes of the lumen cross-sectional area (during the cardiac cycle). (c) A plot describing the time sequence changes of the aorta cross-sectional area. (d). A plot describing the time sequence changes of the thrombus cross-sectional area.

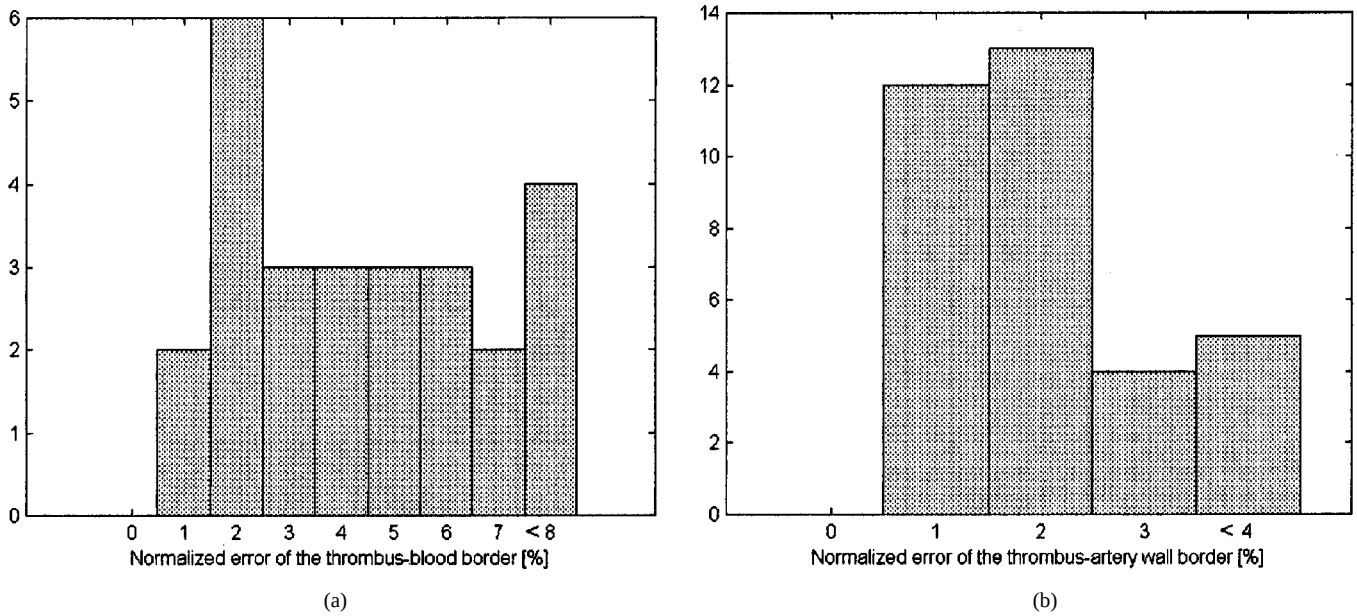

Fig. 3. (a) Histogram of the normalized radial error of identifying the border between the thrombus and the arterial wall. (b) Histogram of the normalized radial error of identifying the border between the thrombus and the blood (lumen).

the present study are compared with this measure (but only for seven sequences out of the 34 cases, which demonstrated reasonable pulsatility): The SD of the length of the border along the aortic cross section circumference (calculated over the sequence of the image frames, i.e., during the cardiac cycle), normalized by the mean (i.e., the mean aortic cross section circum-

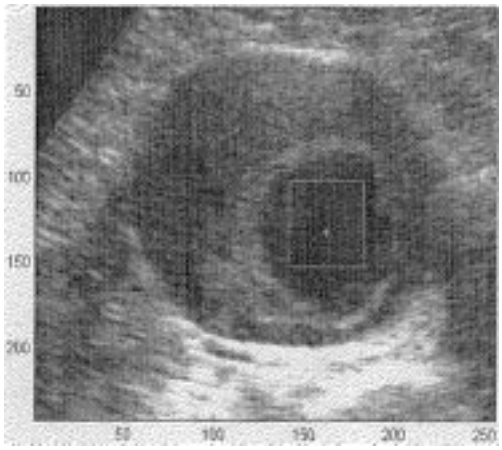

(a)

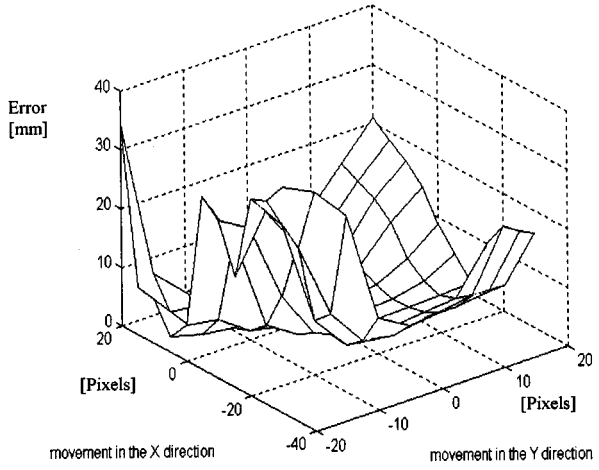

(b)

Fig. 4. Sensitivity of the detection of the border between the thrombus and blood, to movements of the origin. (a) Gray rectangle marks the region in which the origin was moved, with an asterisk marking the origin used to create the reference border. (b) Error (in millimeters) of estimating the border between the thrombus and blood, as calculated by (30), when the origin is being shifted (in pixels), versus the origin being at the center of the lumen.

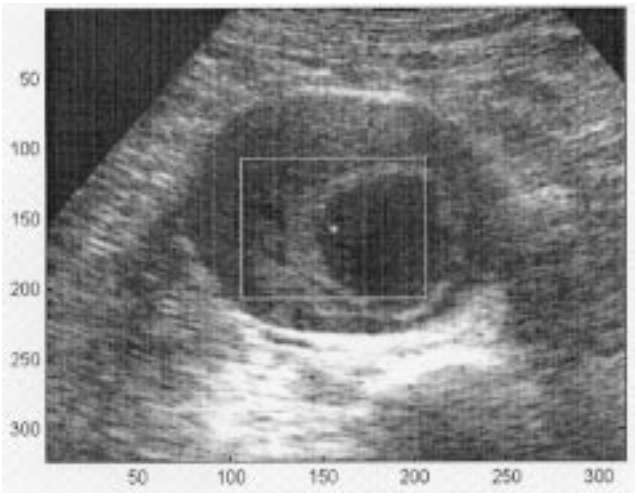

(a)

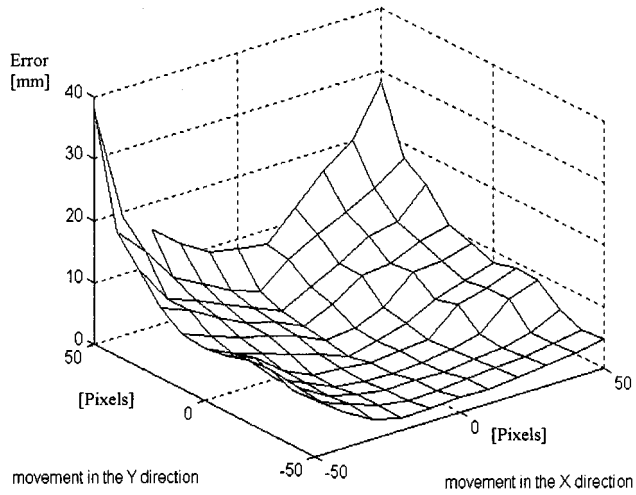

(b)

Fig. 5. Sensitivity of the detection of the border between the thrombus and the arterial wall, to movements of the origin. (a) Gray rectangle marks the region in which the origin was moved, with an asterisk marking the origin used to create the reference border. (b) Error (in millimeters) of estimating the border between the thrombus and arterial wall, as calculated by (30), when the origin is being shifted (in pixels), versus the origin being at the center of the lumen.

ference in that sequence) is compared with the mean diameter of the aorta. The mean diameter of the aorta is calculated by dividing the mean aortic cross section circumference by π. In order to reduce the degradation of the results caused by errors in the SD calculations, an equal number of cardiac cycles is selected. Since no ECG could be measured concurrently with the ultrasound image acquisition–the cardiac cycle lengths are determined from the changes in the aortic cross section area, as calculated from the images [e.g., as seen in Fig. 2(b)]. The results of the pulsatility movement versus the mean aorta diameter are presented in Fig. 6.

The bulging created by the aneurysm is usually asymmetric, and clinical experience indicates that the dorsal part of the arterial wall hardly moves during the cardiac cycle. Thus, it is worth studying the *regional* distension of the wall during the cardiac cycle. A measure is introduced which identifies the sectors that elongate most and that elongate minimally. The size of the sector (angle, in degrees) influences the results (specificity versus sensitivity); a sector of 90° is used as a compromise. The sector is shifted each time by 2°, until a full circle is completed (see Fig. 7). The sector pulsatility movement is calculated each time (i.e., the ratio between the SD of the length of the border along the sector circumference and the mean length, calculated over the sequence of the image frames along the cardiac cycle). The results of these calculated measures are displayed in Fig. 8(a) for the maximal pulsatility movement, and Fig. 8(b) for the minimal pulsatility movement. These two figures demonstrate that some correlation exists between these measures and the diameter of the artery—between the maximal pulsatility movement and the aorta diameter, and between the minimal pulsatility movement and the aorta diameter.

B. Correction of the Angular Divergence Calculation

It is usually assumed that the vector-normal of the true border is radially oriented, thus, the algorithm is based on this assumption. However, this is not always the case and though the orientation is close to that of the radii, it causes errors in calculating the borders. The errors can be reduced by first estimating the orientation of the border, and then performing the divergence

TABLE III
THE ERROR OF ESTIMATING THE BORDER, WHEN THE DIFFERENT PARAMETERS ARE CHANGED BY ±50%. THE ERROR IS CALCULATED IN RELATION TO THE BORDER CALCULATED BY THE PARAMETERS USED FOR PROCESSING ALL THE DATA IN THIS STUDY

The parameter changed	Error of the thrombus – blood border [mm].	Error of the thrombus – artery wall border [mm].
α_{fd} +50%	0.3131	0.0265
α_{fd} −50%	0.3794	0.0647
α_{inf} +50%	0.0096	0.1309
α_{inf} −50%	0.0045	0.0857
α_{rep} +50%	0.3614	0.0016
α_{rep} -50%	$4.3\cdot10^{-8}$	$3.2\cdot10^{-8}$
α_{sd} +50%	0.3257	0
α_{sd} -50%	0.3817	0

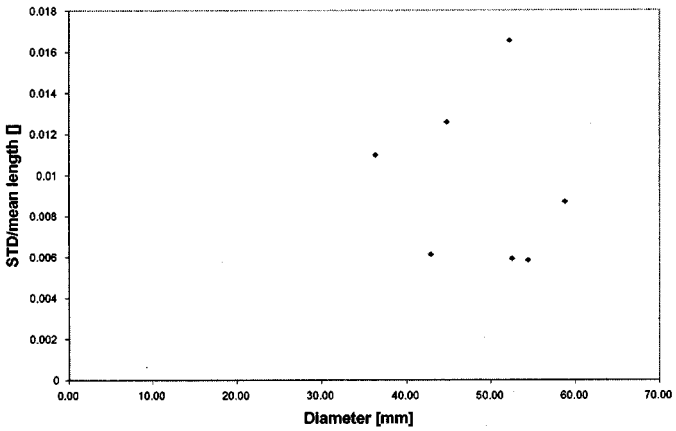

Fig. 6. The SD of the length of the border along the aortic cross section circumference (calculated over the sequence of the image frames, i.e., during the cardiac cycle), normalized by the mean circumference, versus the diameter of the aorta. See text.

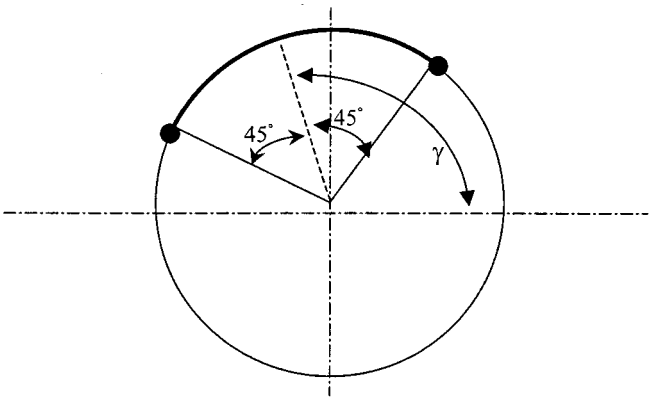

Fig. 7. The sector pulsatility movement is calculated for a 90° sector, with the sector shifting each time by 2°, until a full circle is completed.

operation normal to this border. This can be done by calculating the angle θ_d for each radial (see Fig. 9) and then calculating the normal to the border, using (31):

$$D_1 = G_r \cdot \cos(\theta_d) + G_\theta \cdot \sin(\theta_d) \tag{31}$$

where G_r is the resultant of the edge detection (described in the Section II), and G_θ is the resultant of the same edge detection operation, but applied in the tangential orientation. The remaining parts of the algorithm remain unchanged, except $\psi(m,n)$—the product of the angular divergence (as given in (A.1.6), which is replaced by D_1 above. The results of applying the modified algorithm are compared with those of the original one (see below). An example of the application of the two methods to the same image is given in Fig. 10. The errors associated with the calculation of the borders (of both the border between lumen and thrombus, and the border between the thrombus and arterial wall), when performed by the two algorithms, are depicted in Fig. 11(a), while the Bias is depicted in Fig. 11(b). The differences between the two methods are rather small, usually less than one pixel. The modified algorithm takes into account the cosine of the angle between the normal to the border and the radial, thus, even angles of 30° produce only small differences in the results of the divergence calculations, as performed by the two methods. The results of applying the two methods to three sequences are tabulated in Table IV.

IV. DISCUSSION

The application of the algorithm to 34 different image sequences proved it to be robust and simple, since the algorithm has an explicit formula and only one global minimum. The correlation between the radial distance of the two borders, the one calculated by the original algorithm and the one modified by the correction of the angular divergence, provides also a measure of accuracy and robustness of the method. The correlation coefficient value for the border between the thrombus and the arterial wall reaches 0.9805 ± 0.0113 (when calculated for the last frame in all sequences), and 0.9758 ± 0.0218 for the border between

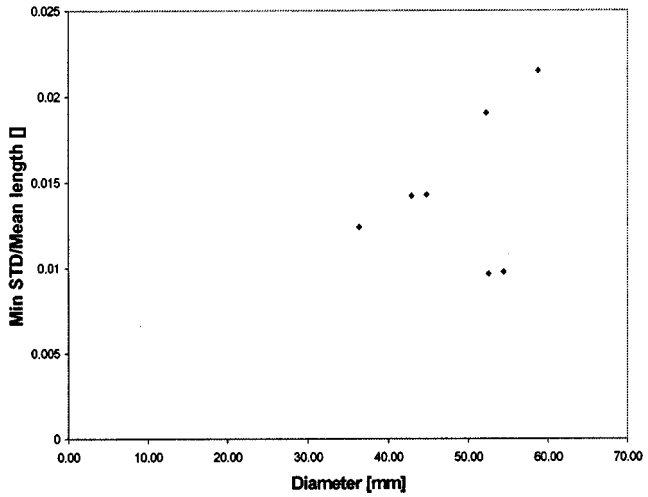

(a)

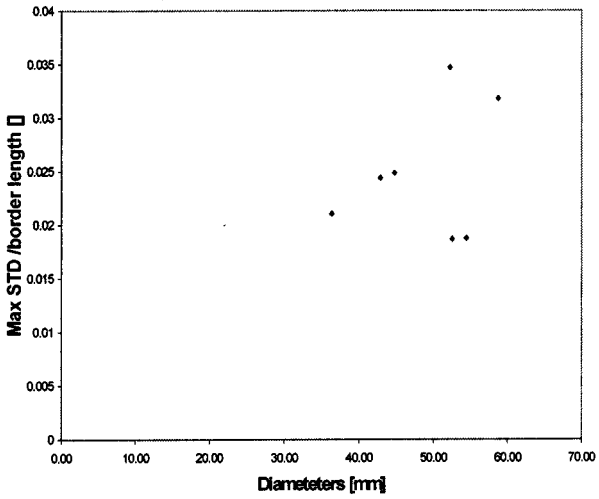

(b)

Fig. 8. (a) Maximal pulsatility movement, and (b) minimal pulsatility movement, calculated by selecting the maximal (and minimal) ratios (between the SD of the length of the border along the sector circumference and the mean length), calculated over the sequence of the image frames along the cardiac cycle.

the lumen and the thrombus. The correlation values for a full sequence of images are depicted in Fig. 12. The modification described above changes the border only slightly. These results are comparable to or better than those found when applying a similar technique to cardiac images in an attempt to detect the endocardial boundary [11].

The algorithm has been validated by several tests. It is insensitive to the selection of the coefficients, as demonstrated above: alterations of $\pm 50\%$ of the value of each coefficient (from the value used for generating all the results above), has no significant effect on the end product—the border, as seen from Table III. The deviations of the calculated borders are small, even for such large changes in coefficient values. As can be seen from Table III, the border between the thrombus and the wall of the artery is the more robust one. The most sensitive parameter is the increase of the "inflation" parameter, which when increased by 50% causes a deviation of 0.13 mm at its extreme value, which is much less than one pixel (as the size of each pixel represents a distance of 0.37 mm).

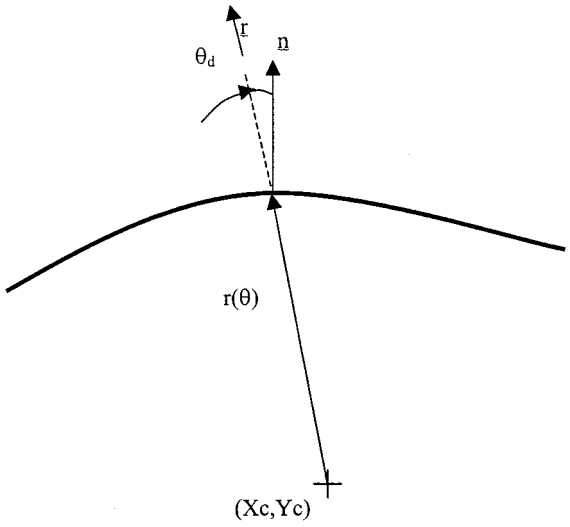

Fig. 9. Correction of the angular divergence calculation: instead of assuming that the normal to this border is performed vector-normal of the true border is in the radial orientation, the angle θ_d between each radial orientation and that of the border orientation is estimated, and then the divergence operation.

The detection of the border between the blood lumen and the thrombus has been also validated. It was found to be more sensitive to perturbation of the coefficients, as can be seen from Table III. This is due to the fact that both the blood region and the thrombus region are characterized by low gray—level values, thus, the SNR of the border is low. There are two moreparameters which are relatively sensitive.

- The first and second derivative coefficients, which are used to increase the robustness of the algorithm to noise in the lumen: Changes of these coefficients, in both directions, cause deviations in estimating the border.
- The increase of the "memory" coefficient also has a significant effect on the solution, as the changes from frame to frame of the lumen area and location may be relatively high.

It must be emphasized, however, that even for the worst case (when the largest border deviation is caused, due to alteration of the coefficients), the deviation is *less than one pixel*.

Another way of validation was performed by shifting the origin of the polar coordinates system, as was demonstrated in Figs. 4 and 5. The sensitivity is specifically low in the case of detection of the border between the thrombus and the arterial wall (Fig. 5), even when the movement of origin shifted it nearly up to the border itself. In the case of the border between the lumen and the thrombus (Fig. 4), the error is somewhat larger, and is not symmetrical. It can be explained by the asymmetrical (elliptic) shape of the lumen, which brings the origin very near to the border itself. The larger error is due also to the high noise levels, especially in the areas near the border. The errors associated with this measurement and detection can be appreciated by studying the error depicted in Fig. 3. The histograms include a large variety of different cases, and also include measurements made at different times during the cardiac cycle. As seen from these histograms, the error of detection of the border between the thrombus and the arterial wall is in most cases under 2%, which is a very good result considering the high noise levels. The error of detection of the border between the lumen and the thrombus is in most cases

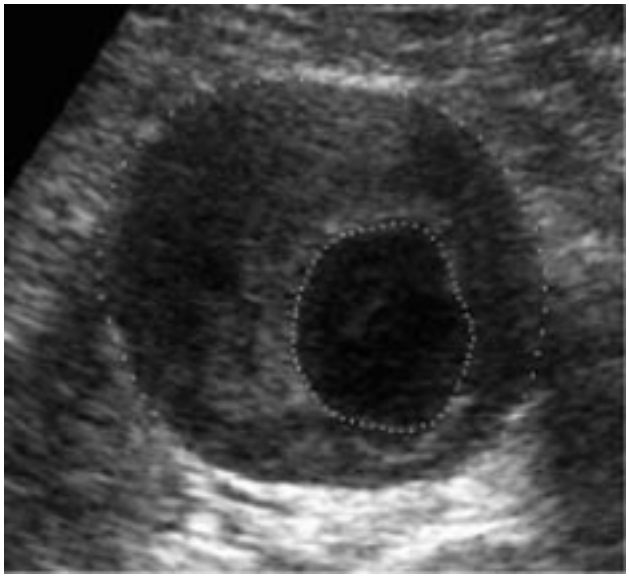

(a)

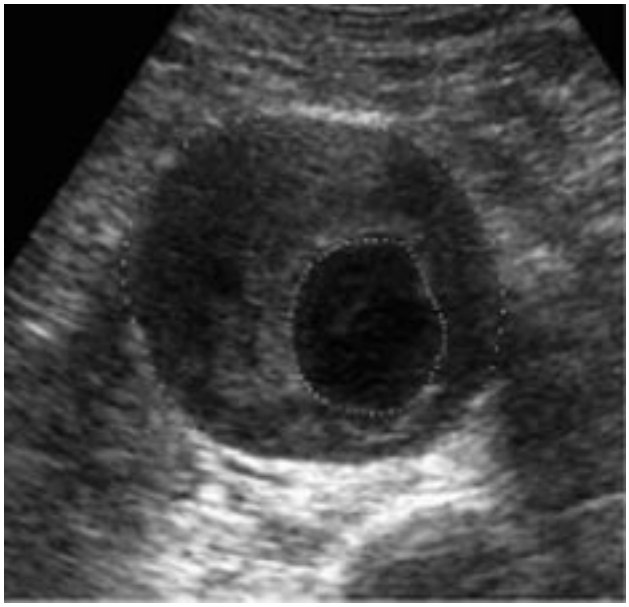

(b)

Fig. 10. (a) An example of applying the modified algorithm is compared with (b) the application of the original one on the same frame.

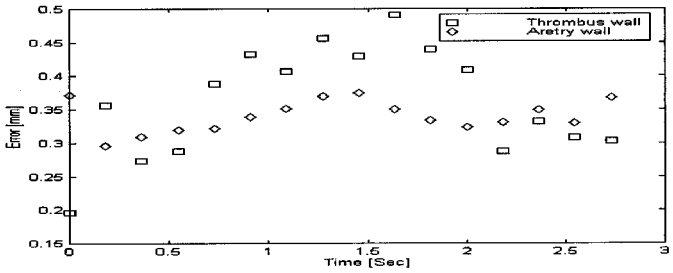

(a)

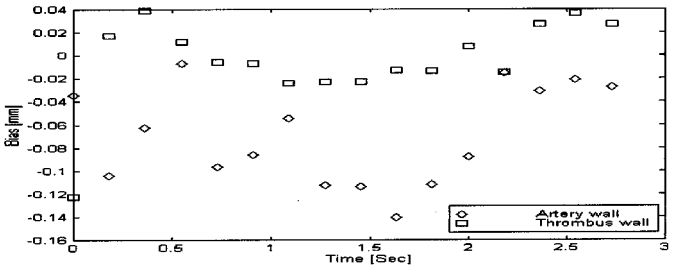

(b)

Fig. 11. (a) The errors associated with the calculation of the borders (for both the border between lumen and thrombus, and the border between the thrombus and arterial wall), when performed by the two algorithms. (b) The bias associated with the same calculations of the borders.

under 4%. This error reached values of 8% due to the sensitivity of the algorithm to noise, caused by the gray level transform described in (27)–(29). These error rates are clinically acceptable since they are lower than those reported for inter-observer variability [30]. The computational complexity of the algorithm is not high: the number of iterations required for convergence of the parameters of the border is much smaller than the number required for the "snakes" algorithm, although the complexity of the calculations within each iteration is higher.

The detection of borders in ultrasound images has been addressed before. An example that succeeds to produce good results is the effort to produce the inner border of the Follicle [28]. It poses a similar problem to the problem posed here of detecting the border between the thrombus and the arterial wall. But the segmentation of the thrombus—blood is a problem of a different nature. Also, the images of the Follicle are acquired by a vaginal probe, which ensures good image quality, and since the distance is short, high-frequency probe (with high resolution) can be used. Patients suffering from Aortic Aneurysm are usually obese, thus, the distance from the probe to the ROI is long, and lower frequencies must be used with lower resolution.

The results presented above, of the method that uses an optimization operation, and the validation of this method, demonstrate the feasibility of automatic measurements of the cross-sectional area and diameter of the abdominal aorta. When AAA exists, the algorithm also allows acceptable measurements of the lumen cross-sectional area and diameter, and the cross-sectional area, of the thrombus. Thus, the customary clinical measurements made frequently in AAA patients, can be made automatically with a high degree of accuracy.

The study of the time dependant changes of these cross-sectional areas during the cardiac cycle is somewhat more limited, because of the extremely small area changes (sometimes less than 1%) in the diseased artery (e.g., AAA). Yet the clinical importance of the measurement obtained here is substantial: the pulsation of the arterial cross-sectional area is evident, even for the severe AAA cases (as those presented here) where the changes are in same order of magnitude as the measurement error. For the less severe cases, the quantification of the area changes is easily measured. Thus, the method can help differentiate between mild AAA cases and severe ones, and possibly keep track of the deterioration. In normal subjects the strain ($\Delta D_{\mathrm{o}}/D_{\mathrm{o}}$ where D_{o} is the diameter and ΔD_{o} is the change of the border) was reported to be in the range 8% in young adults and down to 3% in elderly ($>$60) subjects [23]. The strain may be much smaller in the region of aneurysm, since the incremental circumferential Young's modulus was reported to be more than 250 times that of normal subjects [17]. The attempt to measure changes in area, when the expected changes are so extremely small, is very challenging. It seems, though, that the

TABLE IV
THE DIFFERENCES BETWEEN THE BORDERS AS CALCULATED BY THE MODIFIED ALGORITHM VERSUS THE ORIGINAL ONE, MEASURED AT THE LAST IMAGE OF A SEQUENCE

The image sequence processed	The error at the blood-thrombus border. [Pixels]	The bias at the blood-thrombus border. [Pixels]	The error at the arterial wall-thrombus border. [Pixels]	The bias at the arterial wall-thrombus border. [Pixels]
Sequence I	0.45	0.09	1.16	-0.09
Sequence II	0.5	0.06	0.52	-0.04
Sequence III	1.06	0.17	1.07	0.12

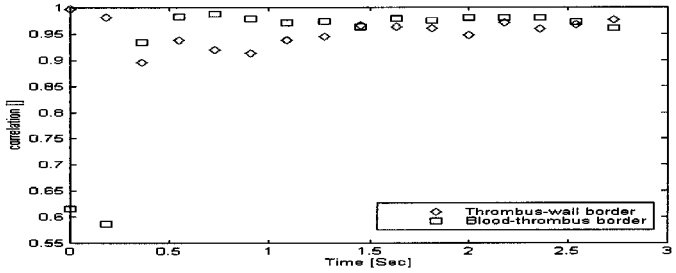

Fig. 12. The correlation values between the radial distance of the border, as calculated by the original algorithm and the modified one for a full sequence of images. It demonstrates the accuracy and robustness of the method.

errors of detecting the arterial wall borders cannot be expected to be reduced by additional processing of the image. Thus, a different approach should be used, e.g., by integrating a mechanical model of the arterial wall as part of the processing of the images. Nevertheless, the method described here provides an automatic and robust method for detection of the lumen and arterial wall, and when the cross-sectional areas bounded by these borders change very little during the cardiac cycle, it may indicate fibrotic wall and higher probability of aortic rupture.

APPENDIX
DESCRIPTION OF THE DERIVATIVE FILTER

This addendum describes an implementation of a convolution with a Gaussian kernel, characterized by a different SD in each direction. This is an IIR recursive implementation especially efficient for large kernels. Since the image given in polar coordinates is described as a nonisotropic field matrix (where the radial and tangential directions are given by different units) the operation of the edge detector must be modified, with the SD of the radial derivative operator different from the SD of tangential smoothing operator. The modified filter is described in (A.1.1)–(A.1.7)

$$\begin{aligned} y_1(m,n) =& a_1 \cdot \mathrm{gr}(m,n) + a_2 \cdot \mathrm{gr}(m,n-1) \\ &+ b_{1,1} \cdot y_1(m,n-1) + b_{2,1} \cdot y_1(m,n-2) \\ n =& 1,\ldots,K; m = 1,\ldots,(R_{\max} - R_{\min} + 1) \end{aligned} \tag{A.1.1}$$

with all the parameters described in (A.1.7). Similarly

$$\begin{aligned} y_2(m,n) =& a_3 \cdot \mathrm{gr}(m,n+1) + a_4 \cdot \mathrm{gr}(m,n+2) \\ &+ b_{1,1} \cdot y_2(m,n+1) + b_{2,1} \cdot y_2(m,n+2) \\ n =& K,\ldots,1; m = (R_{\max} - R_{\min} + 1),\ldots,1 \end{aligned} \tag{A.1.2}$$

y_1 and y_2 represent filtration in the radial direction for both clock-wise and counter clock-wise directions. The image data smoothed radially, by the smoothing operation performed both from the right-hand side (y_1) and the left-hand side (y_2), is described by $\zeta(m,n)$

$$\begin{aligned} \zeta(m,n) =& c_1 \cdot (y_1(m,n) + y_2(m,n)) \\ & n = 1,\ldots,K; m = 1,\ldots,(R_{\max} - R_{\min} + 1). \end{aligned} \tag{A.1.3}$$

The next step is given by defining y_3 and y_4, which represent filtration in the radial direction, from the origin outward and from infinity toward the origin

$$\begin{aligned} y_3(m,n) =& a_5 \cdot \zeta(m,n) + a_6 \cdot \zeta(m-1,n) \\ &+ b_{1,2} \cdot y_1(m-1,n) + b_{2,2} \cdot y_1(m-2,n) \\ n =& 1,\ldots,K; \quad m = 1,\ldots,(R_{\max} - R_{\min} + 1) \end{aligned} \tag{A.1.4}$$

and

$$\begin{aligned} y_4(m,n) =& a_7 \cdot \zeta(m+1,n) + a_8 \cdot \zeta(m+2,n) \\ &+ b_{1,2} \cdot y_2(m+1,n) + b_{1,2} \cdot y_2(m+2,n) \\ n =& K,\ldots,1; \quad m = (R_{\max} - R_{\min} + 1),\ldots,1. \end{aligned} \tag{A.1.5}$$

With all undefined variables set to zero, the result ψ is given by

$$\begin{aligned} \psi(m,n) =& c_2 \cdot (y_3(m,n) + y_4(m,n)) \\ & n = 1,\ldots,K; \quad m = 1,\ldots,(R_{\max} - R_{\min} + 1). \end{aligned} \tag{A.1.6}$$

The constants in these equations are defined, similar to [16]

$$\begin{aligned} & a_1 = 0;\ a_2 = 1;\ a_3 = -1;\ a_4 = 0;\ c_1 = -(1 - e^{-\alpha_{\mathrm{ang}}})^2 \\ & b_{1,1} = 2e^{-\alpha_{\mathrm{ang}}};\quad b_{2,1} = -e^{-2\alpha_{\mathrm{ang}}}; \\ & k = \frac{(1 - e^{-\alpha_{\mathrm{rad}}})^2}{1 + 2\alpha_{\mathrm{rad}} e^{-\alpha_{\mathrm{rad}}} - e^{-2\alpha_{\mathrm{ang}}}} \\ & a_5 = k;\ a_6 = ke^{-\alpha_{\mathrm{rad}}}(\alpha_{\mathrm{rad}} - 1);\ a_7 = ke^{-\alpha_{\mathrm{rad}}}(\alpha_{\mathrm{rad}} + 1) \\ & a_8 = -ke^{-2\alpha_{\mathrm{rad}}};\ c_2 = 1; \\ & b_{1,2} = 2e^{-\alpha_{\mathrm{rad}}};\ b_{2,2} = -e^{-2\alpha_{\mathrm{rad}}} \end{aligned} \tag{A.1.7}$$

where α_{rad} represents the degree of smoothing of the radial derivative, and α_{ang} represents the tangential smoothing. The variables that have not been defined above are set to zero. The

relationship between the parameters α described above and the SD of the kernel are given by [16]

$$\alpha \cdot \sigma = \frac{5}{2\sqrt{\pi}}\alpha. \tag{A.1.8}$$

Since the angles 0 and 2π describe the same point, it was found advantageous to double the angular dimension of the matrix $\mathrm{gr}(m,n)$, so that the image is doubled in one orientation and takes into account the continuity in this orientation.

ACKNOWLEDGMENT

The authors would like to thank GE Medic Systems (Israel) and GE Ultrasound (Israel) for providing the Synergy Ultrasound Imaging system and specifically Dr. Z. Friedman for his continuous support and advice throughout the project.

REFERENCES

[1] D. Adam, O. Hareuveni, and S. Sideman, "Semiautomatic border tracking of cine echocardiographic ventricular images," *IEEE Trans. Med. Imag.*, vol. 6, pp. 266–271, June 1987.

[2] A. A. Amini, T. E. Weymouth, and R. C. Jain, "Using dynamic programming for solving variational problems in vision," *IEEE Trans. Pattern Anal. Machine Intell.*, vol. 12, pp. 855–867, Sept. 1990.

[3] E. Ascher, M. Scheinman, P. DePippo, and W. Yorkovich, "Ruptured versus elective abdominal aortic aneurysm repair: Outcome and cost," *Ann. Vasc. Surg.*, vol. 13, no. (6), pp. 613–617, 1999.

[4] E. Bardinet, L. D. Cohen, and N. Ayache, "Tracking medical 3D data with a deformable parametric model," in *Proc. 3rd Eur3 Conf3 Computer Vision (ECCV'96)*, Cambridge, U.K..

[5] H. G. Beebe and B. Kritpracha, "Screening and preoperative imaging of candidates for conventional repair of abdominal aortic aneurysm," *Sem. Vasc. Surg.*, vol. 12, no. (4), pp. 300–305, 1999.

[6] M. Belkin, M. C. Donaldson, and A. D. Whittemore, "Abdominal aortic aneurysms," *Current Opt. Cardiol.*, vol. 9, pp. 581–590, 1994.

[7] C. J. Bouma, W. J. Niessen, K. J. Zuiderveld, E. J. Gussenhoven, and M. A. Viergever, "Automated lumen definition from 30-MHz intravascular ultrasound images," *Med. Image Anal.*, vol. 1, no. 4, pp. 363–377, 1997.

[8] P. J. Burt and E. H. Adelson, "The Laplacian pyramid as a compact image code," *IEEE Trans. Commun.*, vol. Com-31, no. 4, pp. 532–540, 1983.

[9] J. Canny, "A computational approach to edge detection," *IEEE Trans. Pattern Anal. Machine Intell.*, vol. PAMI-8, no. June, pp. 679–698, 1986.

[10] A. Chakraborty, L. H. Satib, and J. S. Duncan, "Deformable boundary finding in medical images by integrating gradient and region information," *IEEE Trans. Med. Imag.*, vol. 15, pp. 859–870, June 1996.

[11] V. Chalana, D. T. Linker, D. R. Haynor, and Y. Kim, "A multiple active contour model for cardiac boundary detection on echocardiographic sequences," *IEEE Trans. Med. Imag.*, vol. 15, pp. 290–298, June 1996.

[12] M. M. Choy and J. S. Jin, "Extracting endocardial borders from sequential echocardiographic images using mathematical morphology and temporal information to improve contour accuracy," *IEEE Eng. Med. Biol. Mag.*, pp. 116–121, 1998.

[13] L. D. Cohen, "Note on active contour models and balloons," *CVGIP: Image understanding*, vol. 53, no. 2, pp. 211–218, 1991.

[14] L. D. Cohen and I. Cohen, "Finite-element methods for active contour models and balloons for 2-D and 3-D images," *IEEE Trans. Pattern Anal. Machine Intell.*, vol. 15, pp. 1131–1147, Nov. 1993.

[15] J. M. B. Dias and J. M. N. Leitão, "Wall Position and thickness estimation from sequences of echocardiographic images," *IEEE Trans. Med. Imag.*, vol. 15, no. 1, pp. 25–38, 1996.

[16] R. Deriche, "Fast algorithms for low-level vision," *IEEE Trans. Pattern Anal. Machine Intell.*, vol. 12, pp. 78–87, Jan. 1990.

[17] M. Drangova, D. W. Holdsworth, C. J. Boyd, P. J. Dunmore, M. R. Roach, and A. Fenster, "Elasticity and geometry measurements of vascular specimens using a high-resolution laboratory CT scanner," *Physiol. Meas.*, vol. 14, pp. 277–290, 1993.

[18] D. F. Elger, D. M. Blackketter, R. S. Budwig, and K. H. Johansen, "The influence of the shape on the stress in model abdominal aortic aneurysm," *J. Biomech. Eng.*, vol. 18, no. 3, pp. 326–332, 1996.

[19] L. Floreby, "Image analysis and enhancement with application in medicine," Ph.D., Lund Univ., Lund, Sweden, 1998.

[20] N. Friedland and D. Adam, "Automatic ventricular cavity boundary detection from sequential ultrasound images using simulated annealing," *IEEE Trans. Med. Imag.*, vol. 8, pp. 344–353, Aug. 1989.

[21] S. R. Gunn, "Dual active contour models for image feature extraction," Ph.D., University of Southampton, 1996.

[22] E. A. Hoffman. Physiology and function from multidimensional images. presented at Proc. SPIE 2709. [Online]. Available: http://everest.radiology.uiowa.edu/spie/spie/paperaaa/aaa.html

[23] T. Imura, K. Yamamoto, K. Kanamori, T. Mikami, and H. Yasuda, "Noninvasive ultrasonic measurement of the elastic properties of the human abdominal aorta," *Cardiovasc. Res.*, vol. 20, pp. 208–214, 1986.

[24] H. H. S. Ip, R. Hanka, and T. Hongying, "Segmentation of the aorta using temporal active contour model with regularization scheduling," in *Proc. Int. Soc. Opt. Eng.*, vol. 3034, 1997, pp. 323–332.

[25] S. Kalath, P. Tsipouras, and F. H. Silver, "Non-invasive assessment of aortic mechanical property," *Ann. Biomed. Eng.*, vol. 14, pp. 513–524, 1986.

[26] M. Kass, A. Witkin, and S. Terzopoulos, "Snakes: Active contour models," *Int. J. Comput. Vis.*, pp. 321–331, 1988.

[27] D. Kovacevic, S. Loncaric, and E. Sorantin, "Deformable contour based method for medical image segmentation," in *Proc. 21st Int. Conf. Information Technology Interfaces (ITI'99)*, Zagreb, Croatia, 1999, pp. 145–150.

[28] A. Krivanek and M. Sonka, "Ovarian ultrasound image analysis: Follicle segmentation," *Trans. Med. Imag.*, vol. 17, no. 6, pp. 935–944, 1998.

[29] K. F. Lai and R. T. Chin, "Deformable contours: Model and extraction," *IEEE Trans. Pattern Anal. Machine Intell.*, vol. 17, pp. 1084–1090, Nov. 1995.

[30] T. Lanne, T. Sandgren, P. Mangell, B. Sonesson, and F. Hansen, "Improved reliability of ultrasonic surveillance of abdominal aortic aneurysms," *Eur. J. Vasc. Endovasc. Surg.*, vol. 13, pp. 149–153, 1997.

[31] B. Leroy, I. Herlin, and L. D. Cohen, "Multiresolution algorithms for active contour models," in *Proc. 12th Int. Conf. Analysis and Optimization of Systems: Images, Wavelets and PDEs (ICAOS'96)*, Paris, France.

[32] E. Di-Martino, S. Mantero, F. Inzoli, G. Melissano, D. Astore, R. Chiesa, and R. Fumero, "Biomechanics of abdominal aortic aneurysm in the presence of endoluminal thrombus: Experimental characterization and structural static computational analysis," *Eur. J. Vasc. Endovasc. Surg.*, vol. 15, pp. 290–299, 1998.

[33] S. Mallat, "Wavelet of a vision," *Proc. IEEE*, vol. 84, pp. 604–614, Aug. 1996.

[34] M. L. Ragavan, M. W. Webster, and D. A. Vorp, "*Ex vivo* biomechanical behavior of abdominal aortic aneurysm: Assessment using a new mathematical model," *Ann. Biomed. Eng.*, vol. 24, pp. 573–582, 1996.

[35] L. H. Satib and J. S. Duncan, "Boundary finding with parametrical deformable model," *IEEE Trans. Pattern Anal. Machine Intell.*, vol. 14, pp. 1061–1075, Nov. 1992.

[36] B. Solaiman, B. Burdsall, and C. Roux, "Hough transform and uncertainty handling. Application to circular object detection in ultrasound medical images," in *Proc. Int. Conf. Image Processing (ICIP98)*, vol. 3, pp. 828–831.

[37] B. Sonesson, F. Hansen, and T. Lanne, "Abdominal aortic aneurysm: A general defect in the vasculature with focal manifestation in the abdominal aorta," *J. Vasc. Surg.*, pp. 247–254, 1997.

[38] C. Stefanadis, C. Stratos, C. Ylachopoulos, S. Marakas, H. Boudoulas, I. Kallikazaros, E. Tsiamis, K. Toutouzas, L. Sioros, and P. Toutouzas, "Pressure-diameter relation of the human aorta: A new method for determination of the special ultrasonic dimension catheter," *Circulation*, vol. 92, no. 8, pp. 2210–2219, 1995.

[39] R. W. Thompson, "Basic science of abdominal aortic aneurysm: Emerging therapeutic strategies for an unresolved clinical problem," *Curr. Opin. Cardiol.*, vol. 10, pp. 504–518, 1996.

[40] D. A. Vorp, W. A. Mandario, M. W. Webster, and J. Gorcsan III, "Potential influence of intraluminal thrombus on abdominal aortic aneurysm as assessed by a new non invasive method," *Cardiovasc. Surg.*, vol. 4, no. 6, pp. 732–739, 1996.

[41] D. A. Vorp, M. L. Raghavan, and M. W. Webster, "Mechanical wall stress in abdominal aortic aneurysm: Influence of diameter and symmetry," *J. Vasc. Surg.*, vol. 27, no. 4, pp. 632–639, 1998.

[42] A. Yezzi, S. Kichenssamy, A. Kumar, P. Olver, and A. Tennenbaum, "A geometric snake model for segmentation of medical imagery," *IEEE Trans. Med. Imag.*, vol. 16, pp. 199–209, Apr. 1997.

[43] X. Zhang, C. R. McKay, and M. Sonka, "Tissue characterization in intravascular ultrasound images," *IEEE Trans. Med. Imag.*, vol. 17, pp. 880–899, Dec. 1998.